ELSEVIER

Contents lists available at ScienceDirect

## Results in Engineering

journal homepage: www.sciencedirect.com/journal/results-in-engineering



## Research paper

# Dynamic line rating-based routing of overhead transmission lines for wind energy integration

E. Sainz-Ortiz a, R. Martinez a, A. Arroyo a, M. Manana a, S. S. Bustamente a, E. Vejo a

## ARTICLE INFO

#### Keywords: Transmission lines routing Dynamic line rating Wind energy integration Wind simulation Graph theory

#### ABSTRACT

The increasing integration of renewable energy sources, particularly wind power, into the electrical grid presents significant challenges for energy transmission infrastructure. While Dynamic Line Rating (DLR) has emerged as a key technology to enhance the capacity of existing power lines by considering real-time weather conditions, its application in the design of new transmission line routes, especially in complex terrains where wind farms are often located, remains insufficiently investigated. Current route design methodologies, primarily based on Least-Cost Path (LCP) techniques using Geographic Information Systems (GIS), focus on minimizing environmental, technical, and economic costs but neglect the crucial electrical criterion of a line's thermal capacity. Existing attempts to incorporate DLR into route planning have been limited by the use of low-resolution meteorological data and a lack of accurate span modelling, critical for effective DLR implementation.

This paper proposes a novel methodology for designing line routes that integrates DLR to maximize transmission capacity. Our approach addresses the existing research gap by combining micro-scale wind field simulations over complex terrain with a novel raster-based kernel for graph connectivity and span modelling. This method allows for a more precise estimation of wind cooling effects along potential line routes. By integrating GIS tools, wind flow simulations, multi-criteria analysis, and graph theory, this study aims to design routes that not only adhere to traditional constraints but also traverse areas with optimal cooling conditions. The resulting methodology facilitates the development of transmission infrastructures with increased efficiency and capacity, ultimately supporting the large-scale integration of renewable energy.

## 1. Introduction

The reduction of greenhouse gas emissions to prevent a significant increase in global temperatures has led, in recent years, to directives —particularly in Europe— that focus on renewable energy (Renewable Energy Directive [1]), energy efficiency (Energy Efficiency Directive [2]), transportation (Effort Sharing Regulation [3]) and the  $CO_2$  market (Emissions Trading System Directive [4]). These directives involve member countries presenting strategic plans in line with European Union directives, outlining national measures and targets related to energy and climate. A key aspect of these strategic plans is the increase in the use of renewable energy sources, with some countries, such as Denmark, setting targets to achieve 100% renewable electricity generation by 2030 [5]. This not only poses a challenge for the operation of the electrical system but also necessitates investment in electrical infrastructure to efficiently and safely manage electricity from renewable sources.

Renewable resources, especially wind energy, are usually located in mountainous areas such as hills because of their higher wind speed directly related to their energy production. Given this situation, two scenarios usually arise when designing wind plants related to the energy evacuation transmission line.

The first scenario occurs when the local electrical grid often lacks sufficient capacity to absorb the generated energy, leading to the curtailment of renewable energy production—an increasingly recognized challenge that may worsen as renewable penetration grows in the future. This issue can be mitigated through the implementation of various technologies aimed at improving the capacity of the grid.

There are several options to enhance lines capacity. These include the upgrading of existing lines [6] typically using high-temperature low sag conductors [7] or solutions such as the implementation of dynamic line rating (DLR) management systems [8–10]. DLR is a smart grid technology used to estimate the maximum current an overhead line can carry safely without exceeding the conductor's thermal limits (ampacity). The

E-mail address: sainzoe@unican.es (E. Sainz-Ortiz).

https://doi.org/10.1016/j.rineng.2025.107277

Received 23 July 2025; Received in revised form 28 August 2025; Accepted 13 September 2025

<sup>&</sup>lt;sup>a</sup> GTEA research group, Universidad de Cantabria, Santander, Spain

<sup>\*</sup> Corresponding author.

ampacity is influenced by the conductor's properties, installation and operation conditions of the power line (such as maximum operation temperature), and real-time environmental conditions, including ambient temperature, wind speed and wind direction, and solar radiation, as determined by weather stations installed at critical points along the line. Numerous studies [11,12] with sensitivity analysis [13] show that in DLR operation the most influential meteorological variable in the calculation of ampacity is wind direction and speed due to the large forced convection cooling capacity. A key difficulty in implementing DLR systems is to accurately estimate real-time environmental conditions. This issue is aggravated in wind energy integration [14] with complex terrain in which the weather stations are not truly representative of the wind speed and direction due to the large spatial and temporal variability of wind field [15]. Meso-scale weather prediction models with spatial resolution normally in the order of kilometres are unusable for resolving the wind field in complex terrain for DLR management. To address this issue and estimate the wind field at resolutions of micro-scale between 10 and 100 meters, [15,13,16] suggested employing CFD-based simulations to precisely model wind flow over complex terrain, enabling the determination of the cooling profile along the transmission line. In [15], Phillips et al. found that under windy conditions, the transmission line's capacity could increase by 40% to 50%. This is because the strong winds needed for wind energy production also provide natural cooling, thereby enhancing the line's thermal limits and enabling temporary overloading during peak generation periods. References [13,16] highlight that simulating wind fields at the microscale yields valuable insights for identifying critical spans along transmission lines and reinforce the necessity of precise wind direction estimation in DLR applications.

The second scenario arises when the above solutions for increasing line capacity are insufficient or when there are no nearby lines to evacuate the generated energy. This situation creates the need to design a new power line, re-powering the existing line or redesign the route of existing line to increase their capacity.

The design of transmission line route is a complex engineering task involving different procedures aimed at minimizing costs related to operational, technical, environmental and landscape criteria. From technical and operational point of view, the optimal route between two connection points would be a straight line on flat terrain [17,18]. A straight line minimizes the length of the conductor, while allowing the installation of shared suspended towers, avoiding the use of more expensive angled towers. Flat terrain would greatly reduce operational and construction costs, while also allowing towers to be installed with fewer reinforcements due to the high tension generated in conductors with sloping spans.

Nonetheless, the real-world scenario often diverges significantly from this ideal, as the routing of power lines must adhere to various constraints criteria, including rights of way, regulatory issues, the need to avoid sensitive zones like urban areas or nature reserves, and the obligation to maintain safe distances from roads, rivers, buildings, etc., all while minimizing environmental and visual impact. Traditionally, this has been done using Geographic Information Systems (GIS) optimized for processing and visualizing spatial data. One of the most widely studied and used GIS-based techniques in power line route design is known as least-cost path (LCP) [18-23]. This technique uses multi-criteria analysis (MCA) to combine all the criteria mentioned above to generate a raster grid cost surface, where each cell reflects a weighted value indicating the difficulty or resistance associated with traversing that area. Beyond this application, MCA analysis is widely used in complex engineering tasks. In the renewable-energy field, it supports siting and grid-integration studies for wind farms [24] and solar plants [25]. After modelling the cost surface, shortest path algorithms like Dijkstra's [26] are employed to identify the route with the minimum accumulated cost from a source to a destination across the raster grid.

However, the nature of the grid raster in which the space is discretised presents some drawbacks. The routes generated suffer from geometric distortions that result in unnatural routes [27,28]. The re-

sult of these routes is a continuous number of cells in which neither the span nor the position of the towers is modelled, taking into account technical criteria such as the deflection angle between adjacent spans or ground clearances with the terrain. To solve these issues, Piveteau [29] proposed a methodology based on the LCP technique on a graph structure with a cell resolution of 100 m, extending connectivity beyond neighbours adjacent to the cell, limiting the length of the span to a maximum and minimum and taking into account the deflection angle between towers. The author also applied ground clearance restrictions with the terrain. In [30], the author used dynamic programming applied to the Quadratic Shortest Path Problem technique, taking into account the deflection angle, to eliminate distortions and sharp curvatures, creating smoother routes from a design perspective. Nevertheless, the author of this study did not model the span.

At this point, all previous LCP-based techniques for power line route design are based on technical, environmental and landscape criteria, but do not take into account electrical criteria related to DLR. To the best of our knowledge, based on the literature reviewed, only Pytlak and Musilek [31] have incorporated DLR criteria into power line routing design using the LCP technique. However, the authors used meso-scale resolution meteorological data to resolve the wind field, which is insufficient resolution as stated in [15,13,16] for complex terrain, and did not incorporate spatial restrictions such as areas to avoid and ground clearances. One of the major drawbacks of his methodology is the lack of span modelling. As an eight-neighbour rasterised approach was used, the route results in a continuous number of cells, so the effective wind modelling on an entire span lacks physical meaning. This issue is of critical importance, as accurate span modelling is essential for the computation of key variables in systems governed by DLR. In particular, parameters such as effective wind cannot be reliably determined without it, as will be demonstrated in subsequent section

With this in mind, this study aims to fill the gap in the literature on power line route design, taking into account DLR criteria on complex terrain for wind energy integration. To achieve this, a dedicated methodology will be designed to reconstruct the wind field at microscale resolutions, along with the development of a novel raster-based kernel. This kernel facilitates the construction of graph connectivity and span modelling by symmetrically discretizing the spatial propagation directions along the route, thereby enhancing the raster grid resolution and enabling direction-aware processing compatible with effective wind modelling for DLR. The combination of techniques used, including GIS tools, wind flow simulation software, MCA processes, DLR management, and graph theory will allow for the design of electrical line routes that traverse areas with better cooling and, consequently, improving line capacity and optimize the economic efficiency of investments in the development of new power transmission line infrastructure.

## 2. Overhead line routing design based on graph theory

This section presents a detailed description of span modelling and tower positioning based on graph theory, incorporating the proposed raster kernel. It also outlines the spatial constraints to which the graph will be subject.

## 2.1. Graph construction and raster-kernel

In this work, the search space for designing the power line route will be modelled by a graph network. A directed graph  $G = \{V, E\}$  is usually defined as an ordered pair of vertices V (also called nodes) and edges E, where each edge E, defines a connection or relationship between two nodes. As proposed by Piveteau [29], E represents the spans and V the towers. The graph is built by connecting each node with its neighbours and assigning a weight to each edge. For this study, the neighbours will be modelled by the raster kernel, and once the constraints are imposed, the weights are incorporated into the graph structure. This process will be based on a high-resolution digital elevation model (DEM) coordinate

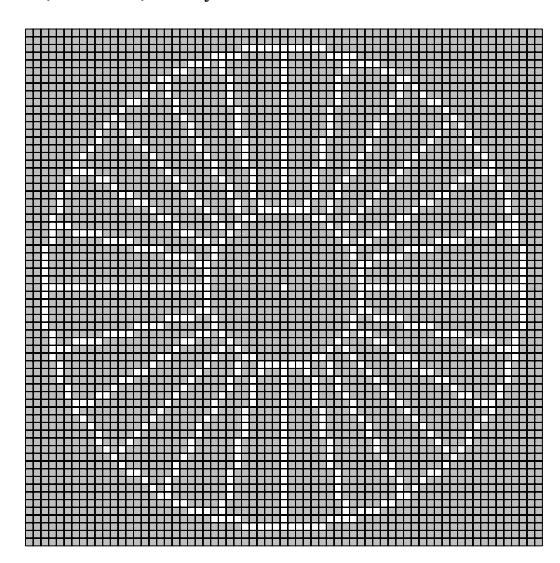


Fig. 1. Raster kernel with 24 span directions.

system, with a cell size of 2 m provided by the Spanish Geographic Institute [32]. The search space where the nodes are located is reduced to a raster grid with a resolution of 25 m using bicubic interpolation. To model the span, the author defined a region as an annulus (circular ring) between a minimum and maximum span length, and enabled the central node connectivity with all neighbours within the annulus with a resolution of 100 m. For this study, the raster kernel was developed to avoid connecting the central node to all nodes in the annulus and to ensure that connectivity is direction-sensitive. This direction-sensitive processing suitable with effective wind modelling for the DLR, allows span directions to be symmetrical in raster space and aligned with the sectors of the wind rose. For kernel modelling, the computer graphics rasterisation algorithms of Bresenham [33] and Andres [34] were used. The algorithm iteratively processes the inner and outer rings to identify the start and end cells of raster lines, ensuring that the imposed directional constraints are symmetrically represented within the raster space, as depicted in the Fig. 1.

The raster kernel offers significant advantages, notably a reduction in computational time for generating connectivity. This is achieved by treating the process as a convolution, *sliding the kernel across the raster space*. Another key benefit is the ability to increase the resolution of the raster where the nodes are defined, as connectivity is assigned only to nodes aligned with the designated propagation directions, thereby avoiding unnecessary connections. Additionally, the kernel ensures symmetry in the propagation directions and allows the number of discrete directions and minimum and maximum span lengths to be varied.

## 2.2. Restricted areas

One of the spatial constraints in power line routing is the presence of restricted areas/zones where construction is limited or prohibited due to environmental, legal, or safety considerations. These include protected natural areas (national parks, nature reserves, etc.), transportation infrastructures (highways, railways, airports, etc.), urban and residential zones (cities, towns, densely populated neighbourhoods, etc.), hydrographic zones (rivers, lakes, etc.), industrial facilities (factories, refineries, etc.), and cultural heritage sites (archaeological zones, monuments, etc.). These constraints were used by [18,21,29,35] and can be divided into two types:

 Areas type 1: Restricted zones where neither transmission towers nor conductors may be installed or suspended, such as urban areas or buildings. Therefore, all nodes within areas 1 will be removed

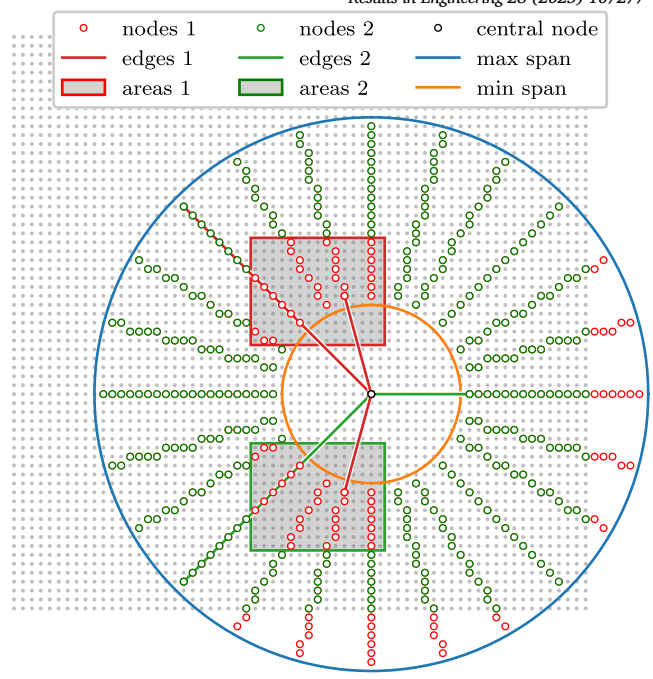


Fig. 2. Graph connectivity and span modelling over raster space.

from the graph, thereby removing their edges. This restriction removes nodes 1 and edges 1 from the graph.

Areas type 2: Restricted zones where the construction of transmission towers is prohibited, although the suspension of conductors is permitted, such as some transport networks or small rivers. This restriction only affects nodes 1, allowing edges 2 to remain in the graph.

The rest of the nodes-edges 2 that remain in the graph are those that are within the minimum and maximum span limits and are not affected by the restriction areas. Nodes out of the raster grid boundaries will be type 1 and will be deleted accordingly. The graph connectivity and span modelling process is illustrated in Fig. 2.

Restricted areas result in node and edge filtering, reducing the complexity of the graph and limiting the search space for the route. They are implemented as computational geometric operations, segment-polygon intersection for edge filtering, and point-in-polygon for node filtering. These operations are computationally expensive because if the search space for the route is in the order of dozens of kilometres, it can contain millions of nodes, dozens of millions of edges and thousands of polygons containing the coordinates of the restrictive areas. To reduce computing time and perform filtering, the Sort-Tile-Recursive (STR) [36] algorithm was used. This algorithm organizes spatial data by sorting and grouping nearby geometries into tiles, creating a spatial index (like an R-tree). This reduces the number of comparisons by limiting intersection tests to nearby geometries. For millions of lines, polygons, and points, STR greatly speeds up the filtering of nodes-edges process.

It should be noted that, in this process, a regulatory safety distance has been applied to restricted areas through a buffer zone. Spatial information for restricted areas was obtained from the Spanish Geographic Institute [37] and the safety and proximity distances are established by Spanish regulations for high voltage power lines RD 223/2008 [38].

## 2.3. Ground clearance

This section details the edge filtering perform to maintain the safety distances between power line conductors and the ground. Spanish regulations RD 223/2008 [38] stipulate that for lines with a voltage level of 132 kV, the minimum safety distance shall be 6.5 m or 7 m when the

Fig. 3. Terrain profile and catenary curves for different conductor temperatures.

lines cross livestock or agricultural holdings. However, 7.5 m is recommended for general design phases, so 7.5 m will be used in this study. It is important to note that during DLR operation, the conductor operates at a higher temperature, which also results in increased sag. To determine safety clearances, the vertical distance between the conductor and the ground surface is evaluated. The terrain profile is generated by interpolating the digital elevation model [32] onto the conductor's projected path, while the conductor's elevation over terrain is computed using the tower heights and the catenary equation.

The general equation of the catenary for levelled spans [39] with vertex (lowest point) at (0,0) is as follows:

$$y(x) = c \cdot \left(\cosh\left(\frac{x}{c}\right) - 1\right) \tag{1}$$

Where c=t/w, is the catenary constant that models the shape of the curve, t is the horizontal component of the tension and w is the conductor weight per unit length. To generalize the equation (1) for level or inclined spans with fixing points  $p_1=(0,y_1)$  and  $p_2=(a,y_2)$  where a is the span length, the equation (1) can be transformed into (4) using the catenary's vertex  $(x_{min},y_{min})$  by means of (2), (3), as illustrated in Fig. 3

$$x_{min} = \frac{a}{2} - c \cdot \operatorname{arcsinh}\left(\frac{y_2 - y_1}{2c \cdot \sinh\left(\frac{a}{2c}\right)}\right)$$
 (2)

$$y_{min} = y_1 - c \cdot \left(\cosh\left(\frac{-x_{min}}{c}\right) - 1\right) \tag{3}$$

$$y(x) = y_{min} + c \cdot \left(\cosh\left(\frac{x - x_{min}}{c}\right) - 1\right) \tag{4}$$

The minimum safety distances are calculated for maximum sag conditions, where the conductor is at their lowest point. To obtain the parameter c for modelling the catenary under maximum sag conditions, the recommendations of CIGRE Technical Brochure 324 [40] and the IEC standard 60826 [41] have been followed, in compliance with Spanish regulations [38]. For this purpose, different loading hypotheses have been applied in accordance with the elevation of the site. The hypotheses apply at different temperatures and include wind, ice, wind combined with ice, EDS (Everyday Stress) and maximum temperature. The hypotheses are implemented with a focus on the most restrictive conditions, ensuring that the resulting tension does not exceed 40–60% of the rated tensile strength (RTS) under the most adverse loading conditions. Between different conditions, the equation of state (5) is used to translate the horizontal tension  $t_1$  obtained in one weather condition to another  $t_2$ .

$$t_2^2 \cdot (t_2 + A) = B \tag{5}$$

The constants A and B are dependent on temperature, span length, overload coefficients, horizontal tensile, modulus of elasticity, expansion coefficient, and conductor cross-section. It should be noted that,

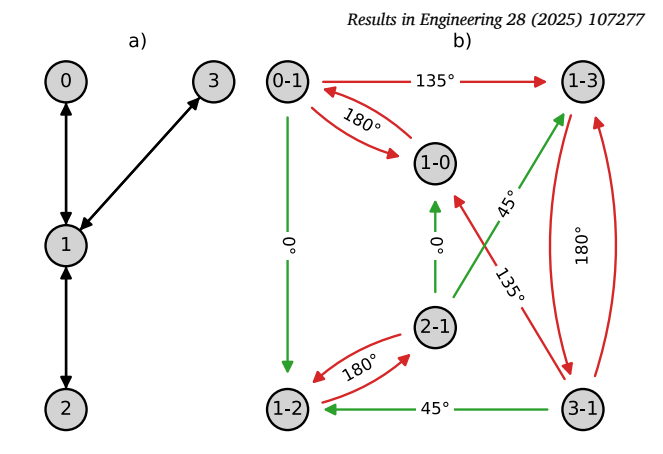


**Fig. 4.** a) Directed graph G. b) Line graph L(G) with angle constraint.

as the line is operated dynamically, the maximum operation conductor temperature will be set. Fig. 3 shows how, as the conductor temperature increases, the catenary sag also increases, resulting in more restrictive safety distances. Finally, the terrain profile plus the safety distance is compared with the catenary at over 250 points. If the catenary is at any point below the safety distance, the edge is removed from the graph and, as a result, the associated span is no longer a candidate for the line route.

#### 2.4. Deflection angle

The last constraint imposed on the graph is the deflection angle. In an electric power line typically refers to the angle between two adjacent spans. Depending on the deflection angle, either suspended or angle towers are required. Suspended towers, which are cost-effective and used for small angles (typically between 0° and 2°) [30], do not carry tensile loads, only suspended ones. Angle towers are structurally more demanding and costly. For larger angles, dead-end towers are employed. To reduce construction costs, the use of suspended towers is maximized by minimizing deflection angles, which also shortens the transmission route. To minimise and limit the deflection angle on the route, the procedure in [29] has been modified to reduce computation times. This procedure consisted of creating a linear graph from the entire original graph and generating the optimal route from the linear graph. Given a graph G its line graph, denoted L(G) [42], is a graph constructed as follows. Each node in L(G) represents an edge in G and two nodes in L(G) are adjacent if and only if their corresponding edges in L(G) share a common node. Since the linear graph structure takes adjacent edges into account, it is suitable for calculating the deflection angle. In this study, it was limited to 60°, as used by Piveteau [29].

Fig. 4.a shows a simplified directed graph, equivalent to the initial graph generated with the raster kernel. The circles represent the nodes (towers), and the bidirectional arrows represent the edges (spans). Fig. 4.b illustrates the line graph of G from Fig. 4.a. Each node in L(G) refers to the origin of the edge in G, and each edge in L(G) contains information about the angle of deflection between two edges in G. Valid edges  $\leq 60^\circ$  are represented by colours. Thus, for example, the edge from 2-1 to 1-3 is a valid connection of 45°, represented in green. However, the edge from 3-1 to 1-0 is not valid (135°), as it exceeds the maximum deflection angle set at 60°. The primary limitation of employing the line graph lies in its inherent complexity. This complexity arises from the linear growth in the number of nodes and an exponential increase in the number of edges. Specifically, given a graph G with  $N_n$  nodes and  $N_e$  edges, the resulting line graph will contain  $N_e$  nodes ( $N_n'$ ) while the number of edges is determined according to equation (6).

$$N_e' = \frac{1}{2} \sum_{i=1}^{N_n} k_i (k_i - 1)$$
 (6)

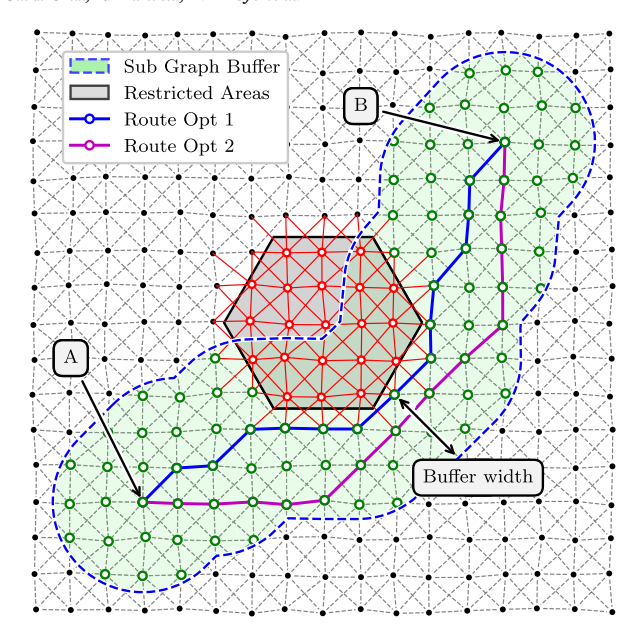


Fig. 5. Two-stage process for obtaining the optimal route.

Where  $k_i$  is the degree of node i and refers to the number of edges connected to node i in G. As can be seen, the number of edges in the line graph increases exponentially with the degree of the nodes in G. This results in high computation times when applying the constraints to the graph and calculating the optimal routes. To solve this problem and increase the graph resolution from 100 m to 25 m as mentioned above, the methodology in [29] was modified, dividing the process into two stages:

- 1. A directed graph G is constructed over the entire search space, incorporating spatial constraints. Edge weights are assigned using a multi-criteria analysis (MCA) that includes the DLR criteria. Subsequently, the optimal route between the designated connection points A-B is determined, referred to as optimal route 1.
- 2. Once the initial optimal route (route 1) is established, a buffer zone (corridor) is generated along its path. Within this buffer, a subgraph sG is constructed, incorporating all nodes and edges from the original graph G that lie within the defined region, while preserving their associated weights. Subsequently, sG is transformed into its corresponding lineal graph, denoted as L(sG), where the deflection angle criteria is integrated into the edge weights. The final optimal route, referred to as optimal route 2, is then computed on this lineal graph representation between A B.

The two-stage process is illustrated in Fig. 5. It should be noted that an 8-neighbour connectivity graph has been used in the representation of Fig. 5, rather than the one generated with the raster kernel, due to the high connectivity, which would generate overlapping edges that would make visualization difficult. A small random spatial deviation has been added to the nodes of this graph to illustrate the correction in the deflection angle. Route 1 prioritizes minimal route length, whereas route 2 optimizes for minimal directional change. It can be seen how route 1 tends to trace the shortest distance between A-B by surrounding the restricted area and using eight changes of direction, while route 2 only makes two changes of direction, making it more suitable for power line design.

## 3. Wind field reconstruction for DLR and ampacity calculation

This section details the simulation of wind fields over complex terrain and how this has been used as a DLR criterion in the design of overhead power line routes.

## 3.1. Wind field modelling based on weather stations data

To estimate the wind field, which involves determining wind speed and direction at micro-scale spatial resolution and low altitudes, the WindNinja simulation software will be used [43,44]. It was developed with the aim of simulating wind propagation to predict fire spread in mountainous areas with complex terrain, making it suitable for this study. The software uses the DEM [32] of the study area and wind conditions as input information to solve the wind field across the entire DEM domain. Minguez et al. [13] used this software to estimate critical spans based on a DLR methodology. However, the method used to drive and initialise the simulation did not use wind data based on local measurements, relying instead on input speeds of 1 m/s and directions from 0° to 359° in 1° intervals. To initialise and drive the simulation in a more accurate and realistic way, the WindNinja point initialisation method was used.

This method allows initialise the simulation with values of wind speed and direction at specified locations and times on the DEM. This information is used to drive the simulation, and the final output wind fields will match the inputs at these locations. Typically, the input information comes from observations at weather stations. For each time step of the simulation, Wind Ninja uses the data from all weather stations and fills the simulation domain horizontally using an inverse distance interpolation method. The domain is then filled vertically using a vertical wind profile, and finally, WindNinja's mass conservation solver computes the wind field over the entire DEM. It should be noted that additional input data must be provided, including the height above ground level of the weather stations and the height of the wind field output.

Once the simulation has been performed, the output wind field is structured into two three-dimensional tensors,  $T_s$  and  $T_d$ , representing the speed s and directions d components of the wind vector field, respectively. Each tensor, defined over dimensions (t,x,y), encapsulates the temporal evolution t of the wind field at each spatial raster cell  $(x_k,y_k)$  defined by the digital elevation model. The entire wind field modelling process is depicted in Fig. 6. In which WindNinja is initialised with three weather stations  $WS_1, WS_2, WS_3$  time series.

## 3.2. Effective wind modelling

Once the wind field has been resolved in the previous section, the variable that models the level of cooling of the line by convection, the effective wind, is calculated. The aim of calculating the effective wind is to obtain the value of the wind perpendicular to the line with the same cooling level as winds with angles of attack different from 90°. The angle of attack is defined as the angle between the wind direction and the longitudinal axis of the conductor. Fig. 7 illustrates the effective wind as a function of wind speed and angle of attack. It can be seen that zero angles of attack (winds parallel to the conductor) result in low effective wind levels and therefore low cooling levels. As the angle of attack increases, the effective wind increases to its maximum value for angle of attack values of 90°, resulting in maximum cooling.

Given that wind demonstrated the most significant influence on the ampacity calculation [13], it was assumed that the line's thermal behaviour was primarily governed by convective cooling due to wind. Based on this assumption, the effective wind speed was estimated to analyse the cooling profile along the transmission line. To compute the effective wind, it is important to analyse Morgan's equations [45]. In [13], a procedure is developed to calculate the effective wind, which results in equation (7).

$$W_{eff} = W \sqrt[n]{M_o} \tag{7}$$

Where  $W_{eff}$  denotes the effective wind speed, W is the actual wind speed,  $M_o$  represents the Morgan coefficient (dependent on the angle of attack  $\alpha$ ) and n is a parameter influenced by the conductor's surface roughness, diameter, and the Reynolds number. The discontinuities observed in Fig. 7 at low speeds arise from the dependence of the parame-

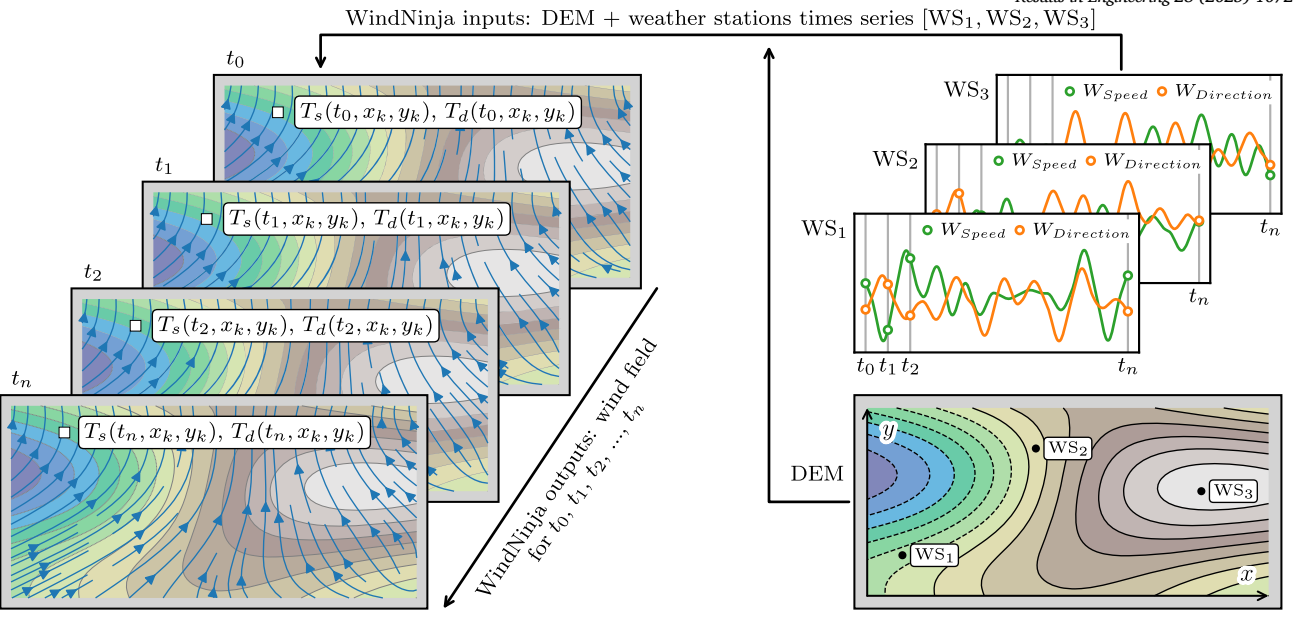


Fig. 6. Wind field modelling process using WindNinja and time series from three weather stations within the study area.

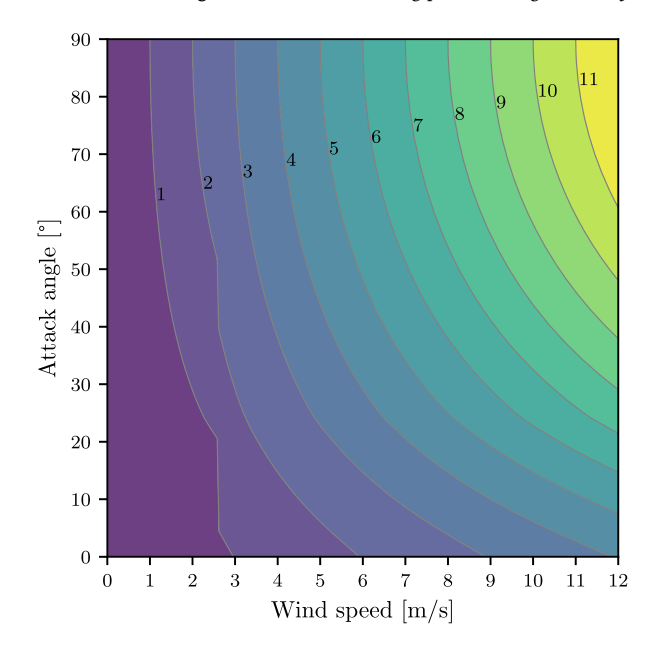


Fig. 7. Effective wind as a function of wind speed and angle of attack.

ter n on the Reynolds number, for which tabulated values are employed. At these speeds, the transition in Reynolds number leads to a discrete change in the corresponding value of n, leading to the discontinuity observed.

To compute the angle of attack  $\alpha$ , it is first necessary to define the unit vectors corresponding to the directions of the conductor and the wind, denoted as  $\vec{C}$  and  $\vec{W}$  respectively. Using Equation (8), evaluate  $\alpha$  such that it lies within the range  $0^{\circ} \le \alpha \le 90^{\circ}$ .

$$\alpha = \min\left[\arccos\left(\vec{C} \cdot \vec{W}\right), 180^{\circ} - \arccos\left(\vec{C} \cdot \vec{W}\right)\right] \tag{8}$$

## 3.3. Ampacity calculation

Once the wind field is characterized and the effective wind speed for each span is obtained, the line ampacity is computed following the methodologies outlined in CIGRÉ Technical Brochure 601 [46] and IEEE Standard 738 [47]. This calculation incorporates time-series data of am-

bient temperature and solar radiation recorded by weather stations. If there is no data of solar radiation it could be estimated from mathematical models based on geographic location and temporal parameters.

## 4. Graph edges weighting process

Edge weighting process involves assigning a cost (numerical value) to represent the resistance to the passage between two connected nodes. The total cost associated with each edge in the graph is computed as a combination of multiple criteria (MCA). Each criteria is individually modelled using a cost function tailored to its specific characteristics, allowing accurate quantification of its contribution to the overall cost. These individual cost components are subsequently integrated through a weighted linear combination, where each cost is scaled by a predefined weight reflecting its relative importance modelled using the Analytical Hierarchy Process (AHP) [48], resulting composite cost value assigned to each edge. Once the total cost has been assigned to all edges, Dijkstra's algorithm [26] is applied to the resulting weighted graph to determine the lowest-cost route between two nodes, enabling efficient and optimized path selection for transmission infrastructure.

The criteria considered in this study are categorized into two types:

- Restricted areas, which represent spatial constraints as described in section 2.2. These constraints lead to the exclusion of specific nodes and edges from the graph, thereby altering its topology and reducing the feasible search space for the optimal route.
- Weight-based criteria, which are used to model the cost associated with each edge. The selected criteria include DLR, deflection angle, span slope and line length.

#### 4.1. Cost functions for weight the criteria

The cost functions presented in this section yield normalized values within the range [0,1], facilitating consistent scaling of each criterion's contribution through assigned weights during final cost computation. Moreover, normalization ensures compatibility with Dijkstra's algorithm, which requires strictly non-negative edge weights to determine the lowest-cost path.

In this work, the cost function associated with the Dynamic Line Rating (DLR) criterion is the only one that incorporates results from the temporal evolution of the wind field presented in section 3. The function

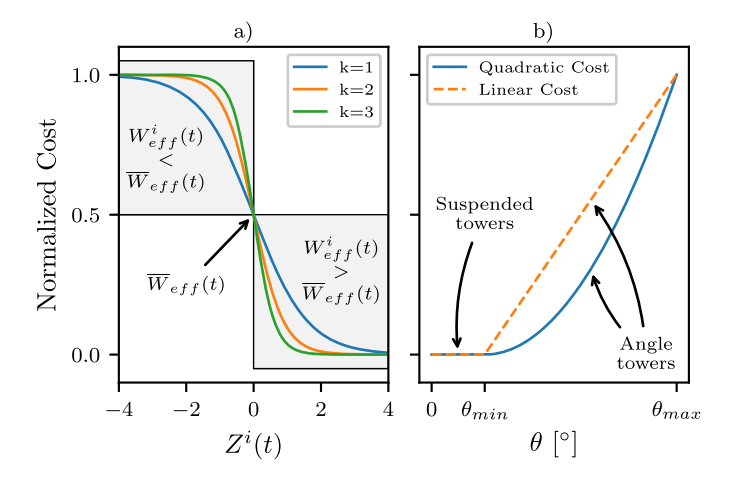


Fig. 8. a) Ampacity cost for a single time step. b) Deflection angle cost.

assigns a cost based on the effective wind  $W_{eff}$ , taking into account for each span its cooling level at each time step (with respect to the rest of the spans) and throughout the entire time domain. The process is carried out in two stages.

In the first stage, equations (9) and (10) are used, for each span i and time step t, the Z-score  $Z^i(t)$  is calculated. This metric provides a measure of the number of standard deviations that a variable deviates from its mean. In this case,  $\overline{W}_{eff}(t)$ ,  $\sigma\big(W_{eff}(t)\big)$  are the mean and standard deviation, respectively, of the effective wind for all spans at time t, and  $W^i_{eff}(t)$  is the effective wind for span i at time t.

$$Z^{i}(t) = \frac{W_{eff}^{i}(t) - \overline{W}_{eff}(t)}{\sigma(W_{eff}(t))}$$

$$(9)$$

Then, the cost  $C^i_{DLR}(t)$  is assigned to each span by means of a non-linear sigmoid function parametrised by k, as shown in Fig. 8 a).

$$C_{DLR}^{i}(t) = \frac{1}{1 + \exp(k \cdot Z^{i}(t))}$$
 (10)

In the second stage (11), the total cost  $C^i_{DLR}$  of each span is calculated by averaging the cost  $C^i_{DLR}(t)$  for the entire time dimension with number of time steps  $N_t$ .

$$C_{DLR}^{i} = \frac{1}{N_t} \sum_{t} C_{DLR}^{i}(t)$$
 (11)

As a result, the cost function assigns higher values to spans with limited cooling capacity and lower values to those with favourable cooling conditions as illustrated in Fig. 8.a. This encourages the routing algorithm to avoid spans with poor cooling and prioritize paths through spans that enhance thermal dissipation. Consequently, the selected route tends to maximize the overall ampacity of the transmission line.

To accurately determine  $W^i_{eff}(t)$ , tensors  $T_s$  and  $T_d$  are first interpolated across 100 discrete points. Subsequently, the angle of attack relative to the span direction is computed at each interpolation point. The effective wind is then identified as the minimum computed value across these points, as this represents the most conservative scenario and thus defines the limiting condition for conductor ampacity. In this context, the discrete directional structure of the raster kernel proposed in section 2.1 enables the interpolation process to be vectorized efficiently. This vectorization significantly reduces computational complexity and runtime, facilitating faster processing and improved scalability in large-scale graphs with millions of edges, such as the one implemented in this work.

For the design of the deflection angle cost function  $C_{\theta}^{i,j}$ , the cost proposed by [30] has been modified. Specifically, the deflection angle interval for suspension towers remains within the range  $[0^{\circ}, \theta_{min}] = [0^{\circ}, 2^{\circ}]$  but the range for angle towers is extended to  $[\theta_{min}, \theta_{max}] = [2^{\circ}, 60^{\circ}]$ . The

introduced modification assigns zero cost to spans employing suspension towers and implements a quadratic cost function for spans requiring angled towers. This approach penalizes angled towers, thus guiding the optimization process toward selecting span sequences whose deflection angles preferentially fall within the specified minimal range, enhancing route efficiency and structural economy. Equation (12) models the proposed  $C_{\theta}^{i,j}$  costs for the deflection angle based on the max function, adding an appropriate slope (linear cost). By squaring (quadratic cost), greater deflection angles are penalised more. This function is illustrated in Fig. 8.b. In  $C_{\theta}^{i,j}$ , the indices i,j represent the cost between the  $span_i$  and  $span_j$ , since this cost is assigned in the linear graph L(G) detailed in section 2.4.

$$C_{\theta}^{i,j} = \left[ \max \left( 0, \frac{\theta - \theta_{min}}{\theta_{max} - \theta_{min}} \right) \right]^2 \tag{12}$$

The cost functions for line length and span slope were developed based on the costs of the methodologies previously presented in [18–20]. The cost for length  $C^i_{length}$  is considered linear, equation (13), where  $span^i$  represents the length of the span i and  $span_{min}$  and  $span_{max}$  are the minimum and maximum lengths for the spans to be determined in the following section.

$$C_{length}^{i} = \frac{span^{i} - span_{min}}{span_{max} - span_{min}}$$
(13)

The cost for the slope of the spans  $C^i_{slope}$  is considered quadratic in equation (14), where  $|slope^i|$  is the absolute value of the slope of the span i and  $slope_{max}$  is the maximum slope allowed, which will be detailed in the following section. This quadratic cost penalizing steeper slopes more severely, reflects the increased structural and economic challenges associated with installing transmission lines over steep terrain, such as higher tower requirements, greater mechanical tension, and increased construction complexity.

$$C_{slope}^{i} = \left(\frac{|slope^{i}|}{slope_{max}}\right)^{2} \tag{14}$$

#### 4.2. Total edge cost

To compute the total cost for each graph edge, we applied the AHP method systematically. Pairwise judgements for the determination of the decision matrix were obtained using the Saaty scale of 1 to 9 from four field experts and the regional Distribution System Operator (DSO). Individual judgements were aggregated into a unified decision matrix, Table 1. The robustness and internal consistency of the judgements were subsequently verified by achieving an acceptable Consistency Ratio (CR < 0.10). The resulting CR was 0.03.

**Table 1**Final decision matrix for the AHP method.

|              | $C_{DLR}$ | $C_{	heta}$ | $C_{slope}$ | $C_{length}$ |
|--------------|-----------|-------------|-------------|--------------|
| $C_{DLR}$    | 1         | 2           | 4           | 5            |
| $C_{	heta}$  | 1/2       | 1           | 2           | 3            |
| $C_{slope}$  | 1/4       | 1/2         | 1           | 3            |
| $C_{length}$ | 1/5       | 1/3         | 1/3         | 1            |

After constructing the AHP decision matrix and deriving the priority vector of weights W, the overall edge cost  $E_C^i$ , for the edge i is obtained as a weighted linear combination of the normalized criterion-costs  $C^i$ , as expressed in (15).

$$E_C^i = \sum_k W_k \cdot C_k^i \tag{15}$$

W = [0.498, 0.260, 0.161, 0.079]

$$C^{i} = [C_{DLR}, C_{\theta}, C_{slope}, C_{length}]$$

In the comparison highlights, the DLR criterion is assigned the highest weight, consistent with the study objective of maximizing ampacity. By contrast, the line length receives a lower weight; nevertheless, prioritizing the deflection angle criterion yields straighter routes with fewer direction changes, thereby indirectly optimizing overall length.

## 5. Case study

This section aims to evaluate the proposed methodology through its application to a real-world power line situated in northwestern Spain. For this purpose, detailed information regarding the line's route, electrical properties, and associated meteorological station data has been made available. The study area encompasses approximately 250  $\rm km^2$  and is characterized by complex topography, with elevations ranging from 400 to 900 meters above sea level.

The power line is the evacuation line of a wind farm. This farm has an installed capacity of 24 MW and is shown in the upper right part of Fig. 9. The line under study, referred to as Line A, extends between *Substation A* and an *Interconnection Point* with another electrical line, designated as Line B as depicted in Fig. 9. Line A has been designed using traditional methods, without the application of graph theory. These methods include the use of GIS technologies, topography, detailed geographical information about the area, and digital elevation models. They also take into account compliance with rights-of-way, as well as environmental and electro-mechanical regulations according to the voltage level. With regard to planning constraints, information on the type of conductor, voltage level, and route coordinates of Line A is available. We implemented constraints based on current regulations, technical standards, and state-of-the-art practices from the literature

Line A operates at a nominal voltage of  $132\,\mathrm{kV}$  and utilizes an LA-280 conductor, identified as 242-AL1/39-ST1A in accordance with UNE-EN 50182. This conductor consists of bare aluminium and with a maximum permissible current of  $581\,\mathrm{A}$  and as mentioned in section 2.3.

To reconstruct the wind field, meteorological data were obtained from three weather stations located at *Substation A*, *Substation B*, and on a tower along Line B, situated between the interconnection point and *Substation B*. The dataset comprised two years of one-minute resolution time series. Samples were excluded when asynchronous measurements occurred between substations due to technical issues. The recorded variables included wind speed, wind direction, and ambient temperature. Solar radiation data is estimated from mathematical models based on geographic location and temporal parameters. These data, in conjunction with the geographic locations of the stations, were used to initialize the WindNinja model, as detailed in Section 3.

For this case study, as described in Sections 2.2, all data concerning restricted areas, rights-of-way, and DEMs were obtained from the Span-

**Table 2**Main variables used in the graphs construction.

| Graph construction and constrains main variables |          |  |  |  |  |
|--|----------|--|--|--|--|
| Graph nodes grid resolution                      | 25 m     |  |  |  |  |
| Base DEM resolution                              | 2 m      |  |  |  |  |
| Graph search space                               | 16x16 km |  |  |  |  |
| Raster kernel directions                         | 24       |  |  |  |  |
| Min span length                                  | 90 m     |  |  |  |  |
| Max span length                                  | 400 m    |  |  |  |  |
| Max span slope                                   | 30%      |  |  |  |  |
| Buffer width for D.angle constraint              | 350 m    |  |  |  |  |
| Max deflection angle for suspended towers        | 2°       |  |  |  |  |
| Max deflection angle for angle towers            | 60°      |  |  |  |  |
| Ground clearance safe distance                   | 7.5 m    |  |  |  |  |
| Towers height                                    | 22 m     |  |  |  |  |
| DLR max temperature                              | 85°C     |  |  |  |  |
| No. interpolations points for ground clearance   | 250      |  |  |  |  |
| No. interpolations points for effective wind     | 100      |  |  |  |  |

ish Geographic Institute [32,37]. The minimum safety and proximity distances considered in this study comply with the requirements established by Spanish regulations for high-voltage power lines 223/2008) [38].

Finally, Table 2 summarizes the main variables used to model the construction and constraints of the graphs. In particular, span-related variables were defined based on the parameters of Line A, with an added variability margin of 10% to enhance the flexibility of the graph within the search space to determine the optimal path.

To select the buffer width variable, the process begins by creating a conservative exploration buffer equal to twice the mean span from Line A, which, when rounded up to the 25 m grid, corresponds to a distance of 450 m. It was observed that, in the final route optimization for deflection angle correction, the line graph did not deviate more than 325 m laterally (for any of the input weights) with respect to the trace of Line G. As a convergence margin, we added one grid cell (+25 m), yielding a 350 m buffer around Line G in stage two. This width preserves all feasible solutions observed while reducing unnecessary search space.

#### 6. Results

This section presents the results obtained using the proposed methodology. To apply Dijkstra's algorithm for determining the optimal route, the end points were defined as the extremes of Line A, the *Interconnection point* and *Substation A*. As described in Section 2.4, the optimization process was conducted in two sequential stages, with the line designations for each stage defined as follows:

- Stage 1: Line G is derived by applying Dijkstra's algorithm to Graph G, which incorporates several criteria, including the DLR criterion.
   To obtain Line A, the optimal value of the parameter k for the C<sup>i</sup><sub>DLR</sub> cost function was identified through a grid search in the range [0.5,6] with a step size of 0.1. The value of k that resulted in the maximum ampacity was identified as k = 5.1.
- Stage 2: Based on the trace of Line G, a buffer zone is generated, within this, a sub-graph sG is generated, from which a corresponding line graph L(sG) is subsequently constructed, as detailed in section 2.4. This graph includes all the criteria used in Graph G and adds the deflection angle criterion. The application of Dijkstra's algorithm to Graph L(sG) yields Line L, which will be used as the final route.

The routes resulting from this study, Line G and Line L, are depicted in Fig. 10. Table 3 presents the filtering of nodes and edges observed in the graphs when various spatial constraints are applied, indicating

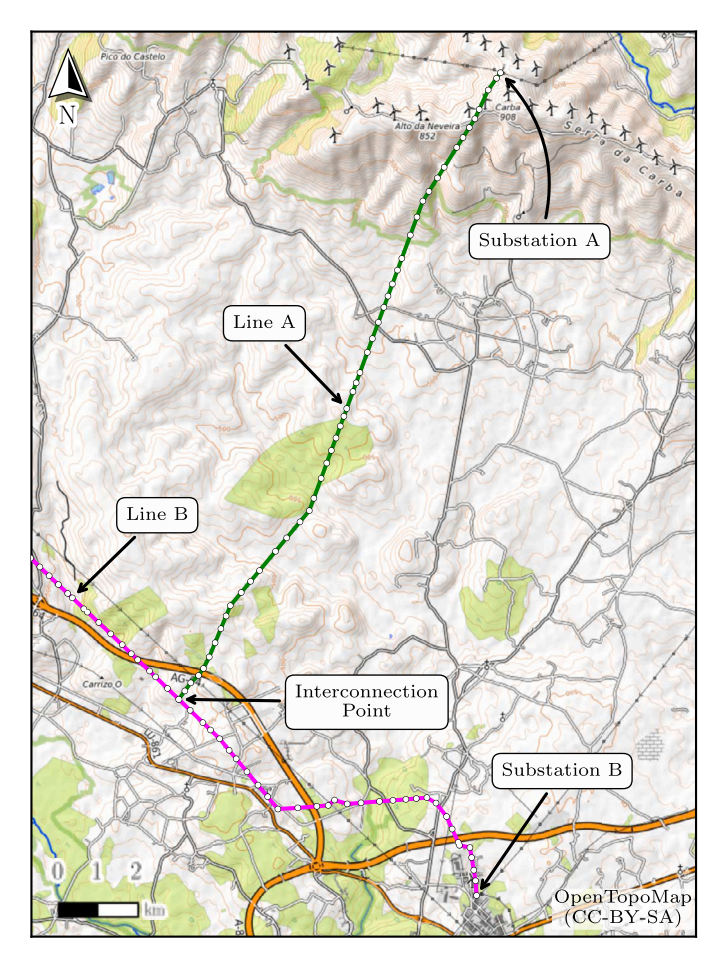


Fig. 9. Study area located in northwestern Spain.

**Table 3** Edge and node filtering across the graphs analysed in this study.

|       |                |                       | Graph constraints: |                  |                  |                       |
|-------|----------------|-----------------------|--------------------|------------------|------------------|-----------------------|
| Graph |                | Initial No.           | Restricted Areas   | Ground Clearance | Deflection Angle | Final No.             |
| G     | Nodes<br>Edges | 234,171<br>8,636,175  | 46,736<br>498,167  | -<br>696,023     | -                | 187,435<br>7,441,985  |
| sG    | Nodes<br>Edges | 8,985<br>588,566      | -                  | -                |                  | 8,985<br>588,566      |
| L(sG) | Nodes<br>Edges | 588,566<br>40,779,682 | -                  | -                | -<br>11,476,172  | 588,566<br>29,303,510 |

both the initial and resulting number of nodes and edges. A dash ("–") denotes the absence of applied restrictions. Notably, the filtered graph L(sG), generated using a buffer of only 350 m in width, contains approximately four times more edges and three times more nodes than the original graph G that covers the full 16x16 km search space. This observation highlights the exponential growth in the structural complexity of graph L(sG) with increasing search area. Consequently, constructing the L(sG) graph across the entire domain becomes computationally infeasible, thereby justifying the use of a two-stage approach for optimal route generation.

Computations were executed on a desktop computer equipped with an Intel Core i7-13700K CPU, 64 GB RAM, and an NVIDIA GeForce RTX 3080 Ti (12 GB) GPU. The two-stage optimization process implemented in Python completed in 12 minutes 35 seconds of elapsed time, and the WindNinja wind-field simulation required 5 hours 40 minutes.

## 6.1. Geometric analysis and span modelling of line Routes

Table 4 presents the results of the geometric modelling of the route and its spans. In terms of total line length, no significant variations were observed across the different configurations. Notably, both the G and L lines exhibit a reduced number of spans compared to the A. This reduction is advantageous, as it implies a lower number of towers required for installation, potentially decreasing construction complexity and associated costs.

Regarding span length, it should be noted that both the minimum and average span lengths on Line G are considerably higher than those observed on lines A and L. However, this disparity is mitigated on Line L, where adjustments lead to a reduction in the difference. The differences in the span slopes among the three lines are within 1%, indicating minimal variation. Among them, Line A demonstrates the most

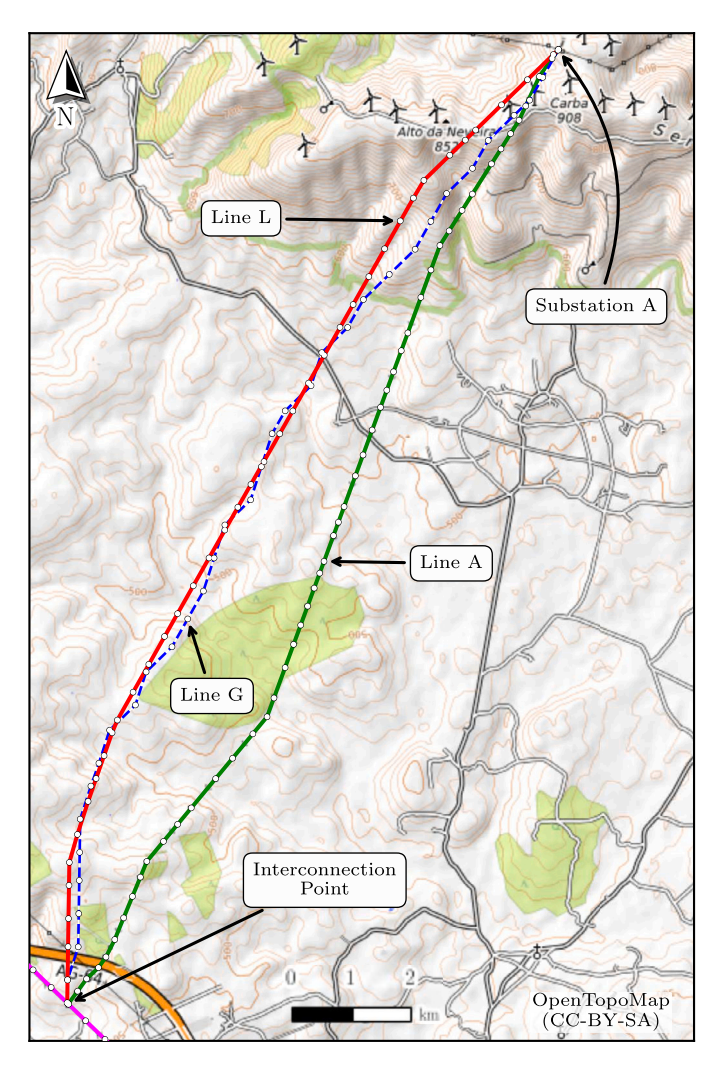


Fig. 10. Transmission line routes resulting in the study area.

Table 4
Results for span modelling.

| Line   | Length<br>(m) | Spans Length<br>(m) |     | Spans Slope<br>(%) |     | Deflection<br>(°) | Deflection Angle (°) |       | Towers<br>No. |       |           |       |
|--------|---------------|---------------------|-----|--------------------|-----|-------------------|----------------------|-------|---------------|-------|-----------|-------|
|        |               | No.                 | min | mean               | max | mean              | max                  | mean  | max           | angle | suspended | angle |
| Line A | 10602         | 49                  | 101 | 216                | 373 | 6.49              | 23.28                | 2.14  | 19.55         | 9     | 39        | 18    |
| Line G | 10874         | 34                  | 212 | 319                | 353 | 6.34              | 25.31                | 12.72 | 27.90         | 21    | 12        | 60    |
| Line L | 10760         | 39                  | 95  | 275                | 353 | 7.30              | 26.36                | 1.28  | 15.96         | 4     | 34        | 10    |

favourable performance, exhibiting the lowest average and maximum slope values.

With respect to the deflection angle, Line G exhibits both high average and maximum values, indicating significant deviation along its path. In contrast, Line L demonstrates an improvement over Line A by reducing these deflection metrics, resulting in a straighter trajectory. This behaviour is illustrated in Fig. 10, where Line G displays a pronounced meandering pattern during its propagation, while Line L follows a more linear course in the vicinity of Line G. This rectification is attributed to the constrained search domain imposed by the previously described buffer. This result identifies Line L as the optimal alternative in terms of deflection angle performance. Specifically, Line L employs only four angle towers representing 10% of the total compared to Line A, which requires nine angle towers, or 18% of its total. The use of a linear graph

is justified by the observation that, starting from a configuration where Line G utilizes 60% of its towers at an angle, a reduction of up to 10% in angled structures is achievable. This reduction enables the use of spans with aligned towers, thereby decreasing both mechanical tension and the more costly angle towers.

## 6.2. Cooling profile along the lines

Fig. 11 (left) presents the simulated wind field and the corresponding cooling profile (bottom right) and angle of attack (top right) for Lines A and L at a representative simulation time step within the studied time domain. Arrows along the line traces indicate the number and positions of transmission towers to facilitate identification of the spans. The results show that Line L maintains a relatively stable angle of attack

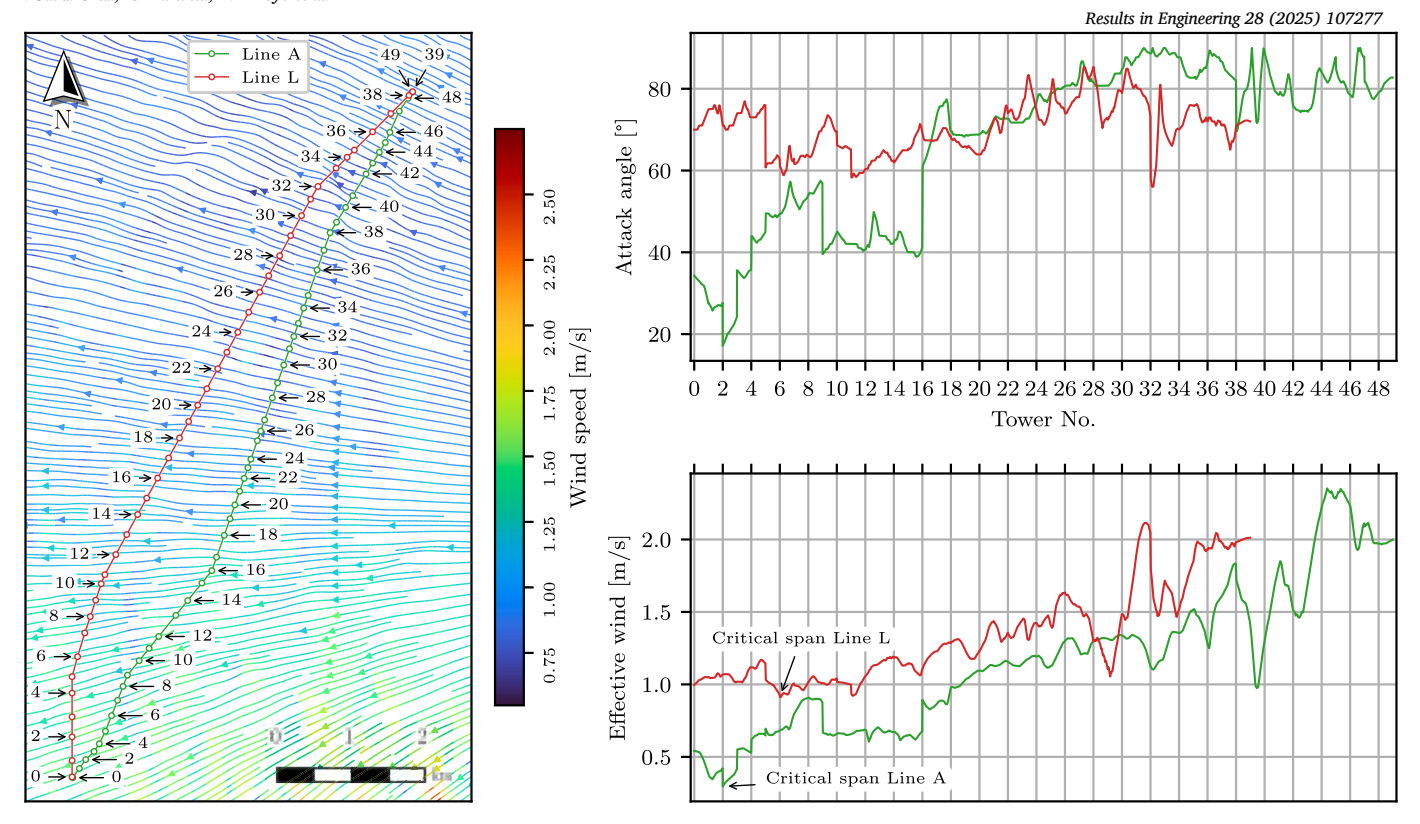


Fig. 11. Cooling profile and angle of attack along the lines.

between approximately 60° and 80°, whereas Line A exhibits a much broader variability. Consequently, the effective wind-based cooling profile reveals that the minimum cooling value, which governs the critical span and thereby the ampacity of the line, is nearly twice as high for Line L compared to Line A and consequently a higher energy transfer capacity within this time step for the Line L. Moreover, due to the design of the DLR cost function described in Section 4.1, this condition is consistently optimized over the entire time domain. In addition, the findings validate the effectiveness of the proposed methodology not only in determining the routing of transmission lines based on thermal performance and ampacity, but also in identifying critical spans along the lines, consistent with the approach described in [13].

## 6.3. Dynamic line rating performance

Once the routes and cooling profiles were analysed, the performance of DLR was assessed. Fig. 12 presents the time series of ampacity values computed for the transmission lines within a region of the simulation domain. For clarity, a Gaussian filter was applied to the time series solely for visualization purposes, this smoothing technique helps reveal overall trends by attenuating high-frequency fluctuations. Importantly, all computational analyses were conducted using the original, unfiltered time series. To calculate the ampacity, the conductor temperature was set to 85 °C and the procedure described in Section 3.3 was used.

Fig. 12 also represents the static ampacity of 581 A determined without the application of the DLR for the selected LA-280 conductor. The ampacity of the three lines consistently exceeds the static limit, as expected given that the calculations were performed under DLR conditions. Notably, Line A, which was not designed with DLR considerations, exhibits lower ampacity values compared to Lines L and G. This is evident in the time-accumulated ampacity graph, where Line G demonstrates the highest cumulative ampacity, followed by Line L. It was anticipated that Line G would achieve higher ampacity values

than Line L, as its routing algorithm is not constrained by deflection angle. This flexibility allows for a more optimized route that maximizes ampacity. Notably, Line L demonstrates the ability to not only surpass Line A in ampacity but also to provide a feasible routing solution with a limited number of angle towers, an advantage not observed in Line G.

Fig. 12 illustrates peaks in power generation that coincide with periods of high wind speed and stability. During these intervals, the difference in transmission capacity between lines designed with DLR criteria with respect to A becomes even more pronounced than under conditions with lower wind resource availability. This relationship is critical for the effective integration of wind energy into the power grid, as periods of elevated wind generation often align with increased demand for transmission line capacity. To quantify this effect, the average power across the entire simulation domain was compared to the generation peaks. These peaks were defined as capacity intervals exceeding 900 A and sustained for a minimum duration of 48 hours. The corresponding results are presented in Table 5.

Two reference metrics were employed:  $\Delta_{abs}$  (L-A), which quantifies the absolute deviation in power of Line L respect to A, and  $\Delta_{\%}$  (L vs A), which expresses this deviation as a percentage. Across the entire domain, Line L exhibited an increase of capacity of 9.2 MW and 5.8%. During peak generation periods, the average improvement is 17.2 MW, corresponding to an increase of 9.28%. These results validate the proposed methodology by demonstrating a significant enhancement in the transmission capacity of Line L across the full temporal domain, including periods of peak generation. This improvement is crucial for reducing renewable energy curtailments, as increased transmission capacity allows for better accommodation of variable generation and minimizes the need to limit output. When expressed in terms of the nominal power of standard utility-scale wind turbines (4.5 MW), the improved performance corresponds to an average increase equivalent to the evacuation capacity of two additional turbines, and up to three to four turbines during peak generation periods.

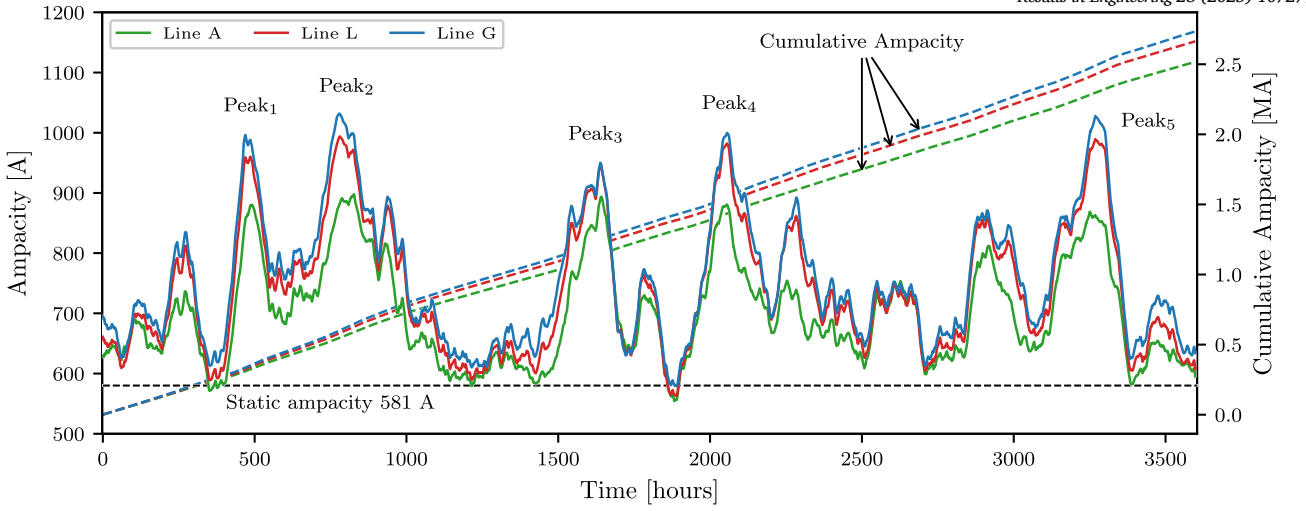


Fig. 12. Ampacity time series.

Table 5
Results for DLR.

|                          | Average power transmission capacity (MW) |         |         |         |         |         |  |  |  |
|--------------------------|--|---------|---------|---------|---------|---------|--|--|--|
| Simulation Period        | All domain                               | Peak 1  | Peak 2  | Peak 3  | Peak 4  | Peak 5  |  |  |  |
| Line G                   | 173.171                                  | 201.586 | 216.513 | 203.049 | 206.264 | 215.747 |  |  |  |
| Line L                   | 168.638                                  | 192.830 | 208.122 | 200.183 | 203.938 | 211.324 |  |  |  |
| Line A                   | 159.395                                  | 172.480 | 189.424 | 185.113 | 188.236 | 195.206 |  |  |  |
| $\Delta_{\rm abs}$ (L-A) | 9.243                                    | 20.350  | 18.698  | 15.070  | 15.702  | 16.118  |  |  |  |
| $\Delta_{\%}$ (L vs A)   | 5.799%                                   | 11.799% | 9.871%  | 8.141%  | 8.342%  | 8.257%  |  |  |  |

#### 7. Conclusions

This study has successfully developed and validated a novel methodology for designing power transmission line routes by integrating high-resolution, micro-scale wind field simulations with DLR criteria into a GIS-based framework. The proposed approach overcomes critical limitations of existing route design methods, which have traditionally neglected the thermal capacity of conductors, by explicitly optimizing for wind-induced cooling to maximize ampacity.

The results demonstrate the effectiveness of a two-stage optimization strategy. The initial stage identifies a buffer zone with optimal cooling conditions (Line G), while the second stage refines this path to produce a geometrically feasible and cost-effective route (Line L) by incorporating engineering constraints such as deflection angles. This two-stage process was proven to be essential for managing the computational complexity that would arise from applying a detailed angle constrain across the entire search space.

A comparative analysis showed that the final optimized route, (Line L), offers significant advantages over a conventionally designed route (Line A). Geometrically, Line L requires fewer support towers and substantially reduces the number of expensive angle towers from 18% of the total to just 10%. Electrically, the strategic routing of Line L through areas with more favourable wind conditions results in a minimum cooling value nearly double that of Line A, which is the critical factor determining the line's overall ampacity.

Quantitatively, this improved thermal performance translates into a significant increase in transmission capacity. Line L demonstrated an average ampacity increase of 5.8% over the baseline, with this advantage rising to 9.28% during peak wind generation periods. This enhancement is critical for mitigating the curtailment of renewable energy, as it directly aligns increased transmission capacity with periods of high energy production. In practical terms, the increased capacity is equivalent to accommodating the power output of two additional utility-scale wind turbines on average, and up to four turbines during peak conditions.

An additional benefit of the line route optimization is the extension of the conductor's service life. By ensuring more effective cooling, the methodology leads to lower operating temperatures at sub-maximal loads, which in turn reduces the cumulative thermal stress and degradation of the conductor over its lifespan.

In summary, the methodology presented provides a robust and practical framework for designing the next generation of transmission line infrastructure. By integrating DLR principles at the design stage, it enables the creation of more efficient, cost-effective, and higher-capacity power lines, thereby facilitating the large-scale integration of renewable energy sources into the electrical grid.

## CRediT authorship contribution statement

E. Sainz-Ortiz: Writing – review & editing, Writing – original draft, Visualization, Validation, Software, Methodology, Investigation, Formal analysis, Conceptualization. R. Martinez: Writing – review & editing, Writing – original draft, Validation, Supervision, Software, Methodology, Data curation. A. Arroyo: Writing – review & editing, Validation, Supervision, Methodology. M. Manana: Writing – review & editing, Validation, Supervision, Software, Project administration, Methodology, Funding acquisition. S. Bustamente: Writing – review & editing, Validation, Methodology. L. Vejo: Writing – review & editing, Validation.

#### Declaration of competing interest

The authors declare that they have no known competing financial interests or personal relationships that could have appeared to influence the work reported in this paper.

## Acknowledgements

This research was partially supported by Spanish Government Grant PID2023-151457OB-I00 funded by MICIU/ AEI/ 10.13039/

501100011033 and, as appropriate, by "ERDF A way of making Europe", by "ERDF/EU", by the "European Union" or by the "European Union NextGenerationEU/PRTR".

## Data availability

The authors do not have permission to share data.

#### References

- [1] European Parliament and Council of the European Union, Directive (EU) 2023/2413 of the European Parliament and of the Council of 18 October 2023 amending Directive (EU) 2018/2001, Regulation (EU) 2018/1999 and Directive 98/70/EC as regards the promotion of energy from renewable sources, and repealing Council Directive (EU) 2015/652, https://eur-lex.europa.eu/eli/dir/2023/2413/oj, October 2023, official Journal of the European Union, L 2023/2413.
- [2] European Parliament and Council of the European Union, Directive (EU) 2023/1791 of the European Parliament and of the Council of 13 September 2023 on energy efficiency (recast), https://eur-lex.europa.eu/eli/dir/2023/1791/oj, September 2023, official Journal of the European Union, L 231, 20.9.2023, p. 1–114.
- [3] European Parliament and Council of the European Union, Regulation (EU) 2023/857 of the European Parliament and of the Council of 19 April 2023 amending Regulation (EU) 2018/842 on binding annual greenhouse gas emission reductions by Member States from 2021 to 2030 contributing to climate action to meet commitments under the Paris Agreement, https://eur-lex.europa.eu/eli/reg/2023/857/oj, April 2023, official Journal of the European Union, L 111, 26.4.2023, p. 1–7.
- [4] European Parliament and Council of the European Union, Directive (EU) 2023/959 of the European Parliament and of the Council of 20 April 2023 amending Directive 2003/87/EC establishing a system for greenhouse gas emission allowance trading within the Union, for the period 2024 to 2030, https://eur-lex.europa.eu/eli/dir/2023/959/oj, April 2023, official Journal of the European Union, L 132, 21.4.2023, p. 1–68.
- [5] Danish Ministry of Climate, Energy and Utilities, Denmark's Integrated National Energy and Climate Plan, https://ens.dk/en/our-services/energy-planning/nationalenergy-and-climate-plans, 2020. (Accessed 7 July 2025).
- [6] N. Mbuli, R. Xezile, L. Motsoeneng, M. Ntuli, J.-H. Pretorius, A literature review on capacity uprate of transmission lines: 2008 to 2018, Electr. Power Syst. Res. 170 (2019) 215–221, https://doi.org/10.1016/j.epsr.2019.01.006, https://www. sciencedirect.com/science/article/pii/S0378779619300124.
- [7] P. Parvizi, M. Jalilian, K.D. Dearn, Evaluating the mechanical and thermal performance of high-temperature low sag (htls) conductors: a comparative study of accc, acss, and acsr conductors, Results Eng. 26 (2025) 104735, https://doi.org/10.1016/j.rineng.2025.104735, https://www.sciencedirect.com/science/article/pii/S2590123025008126.
- [8] D.L. Alvarez, J.A. Rosero, F. Faria da Silva, C.L. Bak, E.E. Mombello, Dynamic line rating — technologies and challenges of pmu on overhead lines: a survey, in: 2016 51st International Universities Power Engineering Conference (UPEC), 2016, pp. 1–6.
- [9] S. Uski, Estimation method for dynamic line rating potential and economic benefits, Int. J. Electr. Power Energy Syst. 65 (2015) 76–82, https://doi.org/ 10.1016/j.ijepes.2014.09.034, https://www.sciencedirect.com/science/article/pii/ S0142061514005857.
- [10] D.A. Douglass, J. Gentle, H.-M. Nguyen, W. Chisholm, C. Xu, T. Goodwin, H. Chen, S. Nuthalapati, N. Hurst, I. Grant, J.A. Jardini, R. Kluge, P. Traynor, C. Davis, A review of dynamic thermal line rating methods with forecasting, IEEE Trans. Power Deliv. 34 (6) (2019) 2100–2109, https://doi.org/10.1109/TPWRD.2019.2932054.
- [11] Y.-Q. Ding, M. Gao, Y. Li, T.-L. Wang, H.-L. Ni, X.-D. Liu, Z. Chen, Q.-H. Zhan, C. Hu, The effect of calculated wind speed on the capacity of dynamic line rating, in: 2016 IEEE International Conference on High Voltage Engineering and Application (ICHVE), 2016, pp. 1–5, https://ieeexplore.ieee.org/document/7800912.
- [12] J. Fu, S. Abbott, B. Fox, D.J. Morrow, S. Abdelkader, Wind cooling effect on dynamic overhead line ratings, in: 45th International Universities Power Engineering Conference UPEC2010, 2010, pp. 1–6.
- [13] R. Minguez, R. Martinez, M. Manana, D. Cuasante, R. Garañeda, Application of digital elevation models to wind estimation for dynamic line rating, Int. J. Electr. Power Energy Syst. 134 (2022) 107338, https://doi.org/10.1016/j.ijepes.2021.107338, https://www.sciencedirect.com/science/article/pii/S0142061521005779.
- [14] E. Fernandez, I. Albizu, M. Bedialauneta, A. Mazon, P. Leite, Review of dynamic line rating systems for wind power integration, Renew. Sustain. Energy Rev. 53 (2016) 80–92, https://doi.org/10.1016/j.rser.2015.07.149, https://www.sciencedirect.com/science/article/pii/S1364032115007960.
- [15] T. Phillips, R. DeLeon, I. Senocak, Dynamic rating of overhead transmission lines over complex terrain using a large-eddy simulation paradigm, Renew. Energy 108 (2017) 380–389, https://doi.org/10.1016/j.renene.2017.02.072, https://www. sciencedirect.com/science/article/pii/S0960148117301581.
- [16] A.W. Abboud, J.P. Gentle, T.R. McJunkin, J.P. Lehmer, Using computational fluid dynamics of wind simulations coupled with weather data to calculate dynamic line ratings, IEEE Trans. Power Deliv. 35 (2) (2020) 745–753, https://doi.org/10.1109/ TPWRD.2019.2925520.

- [17] F. Kiessling, P. Nefzger, J.F. Nolasco, U. Kaintzyk, Overhead Power Lines: Planning, Design, Construction, Springer, 2014.
- [18] A.H.M. Santos, R.M. de Lima, C.R.S. Pereira, R. Osis, G.O.S. Medeiros, A.R. de Queiroz, B.K. Flauzino, A.R.P.C. Cardoso, L. Czank Junior, R.A. dos Santos, E.L. Carvalho Junior, Optimizing routing and tower spotting of electricity transmission lines: an integration of geographical data and engineering aspects into decision-making, Electr. Power Syst. Res. 176 (2019) 105953, https://doi.org/10.1016/j.epsr.2019. 105953, https://www.sciencedirect.com/science/article/pii/S037877961930272X.
- [19] R.M. de Lima, R. Osis, A.R. de Queiroz, A.H.M. Santos, Least-cost path analysis and multi-criteria assessment for routing electricity transmission lines, IET Gener. Transm. Distrib. 10 (16) (2016) 4222–4230, https:// doi.org/10.1049/iet-gtd.2016.1119, https://ietresearch.onlinelibrary.wiley.com/ doi/pdf/10.1049/iet-gtd.2016.1119, https://ietresearch.onlinelibrary.wiley.com/ doi/abs/10.1049/iet-gtd.2016.1119.
- [20] C. Monteiro, I. Ramirez-Rosado, V. Miranda, P. Zorzano-Santamaria, E. Garcia-Garrido, L. Fernandez-Jimenez, GIS spatial analysis applied to electric line routing optimization, IEEE Trans. Power Deliv. 20 (2) (2005) 934–942, https://doi.org/10.1109/TPWRD.2004.839724, https://ieeexplore.ieee.org/document/1413336.
- [21] S. Bagli, D. Geneletti, F. Orsi, Routeing of power lines through least-cost path analysis and multicriteria evaluation to minimise environmental impacts, Environ. Impact. Asses. Rev. 31 (3) (2011) 234–239, https://doi.org/10.1016/j.eiar.2010.10.003, https://www.sciencedirect.com/science/article/pii/S0195925510001393.
- [22] D. Bachmann, F. Bökler, J. Kopec, K. Popp, B. Schwarze, F. Weichert, Multi-objective optimisation based planning of power-line grid expansions, ISPRS Int. J. Geo-Inf. 7 (7) (2018) 258, https://doi.org/10.3390/ijgi7070258, Publisher: Multidisciplinary Digital Publishing Institute https://www.mdpi.com/2220-9964/7/7/258.
- [23] S. Ghandehari Shandiz, G. Doluweera, W.D. Rosehart, L. Behjat, J.A. Bergerson, Investigation of different methods to generate power transmission line routes, Electr. Power Syst. Res. 165 (2018) 110–119, https://doi.org/10.1016/j.epsr.2018.08.012, https://www.sciencedirect.com/science/article/pii/S0378779618302554.
- [24] I.F. Fotsing Metegam, I.Y. Bomeni, V.S. Chara-Dackou, D. Njomo, R. Tchinda, Technical and geographic potential analysis for large-scale wind energy production using a gis-ahp multi-criteria in Cameroon, Results Eng. 24 (2024) 102765, https://doi.org/10.1016/j.rineng.2024.102765, https:// www.sciencedirect.com/science/article/pii/S259012302401020X.
- [25] S. Hosouli, R.A. Hassani, Application of multi-criteria decision making (mcdm) model for solar plant location selection, Results Eng. 24 (2024) 103162, https://doi.org/10.1016/j.rineng.2024.103162, https://www.sciencedirect.com/science/article/pii/S2590123024014178.
- [26] E.W. Dijkstra, A note on two problems in connexion with graphs, Numer. Math. 1 (1) (1959) 269–271, https://doi.org/10.1007/BF01386390.
- [27] D.L. Huber, R.L. Church, Transmission corridor location modeling, J. Transp. Eng. 111 (2) (1985) 114–130, https://doi.org/10.1061/(ASCE)0733-947X(1985) 111:2(114), publisher: American Society of Civil Engineers, https://ascelibrary.org/doi/10.1061/(ASCE)0733-947X(1985)111:2(114).
- [28] T. Shirabe, On distortion of raster-based least-cost corridors, in: J.A. Miller, D. O'-Sullivan, N. Wiegand (Eds.), Geographic Information Science, Springer International Publishing, Cham, 2016, pp. 101–113.
- [29] N. Piveteau, J. Schito, M. Raubal, R. Weibel, A novel approach to the routing problem of overhead transmission lines, Ph.D. thesis, Geographic Information Science University of Zurich Institute of Cartography and Geoinformation ETH, Zurich, 2017.
- [30] J. Vilela, B. Fanzeres, R. Martinelli, R. Moreno, A holistic methodology to identify cost-effective smooth routes for power transmission lines, IEEE Trans. Power Syst. 38 (4) (2023) 3504–3513, https://doi.org/10.1109/TPWRS.2022.3207666.
- [31] P. Pytlak, P. Musilek, An intelligent weather-based system to support optimal routing of power transmission lines, in: 2010 IEEE Electrical Power & Energy Conference, 2010, pp. 1–6.
- [32] Instituto Geográfico Nacional (IGN), Centro Nacional de Información Geográfica (CNIG), Modelo Digital del Terreno 2ª Cobertura MDT02, https://centrodedescargas. cnig.es/CentroDescargas/modelo-digital-terreno-mdt02-segunda-cobertura, 2025.
- [33] J.E. Bresenham, Algorithm for computer control of a digital plotter, IBM Syst. J. 4 (1) (1965) 25–30, https://doi.org/10.1147/sj.41.0025.
- [34] E. Andres, Discrete circles, rings and spheres, Comput. Graph. 18 (5) (1994) 695–706, https://doi.org/10.1016/0097-8493(94)90164-3, https://www.sciencedirect.com/science/article/pii/0097849394901643.
- [35] G. Houston, C. Johnson, EPRI-GTC Overhead Electric Transmission Line Siting Methodology, Technical Report 1013080, Electric Power Research Institute and Georgia Transmission Corporation, Palo Alto, CA and Tucker, GA (USA), 2006.
- [36] S. Leutenegger, M. Lopez, J. Edgington, Str: a simple and efficient algorithm for r-tree packing, in: Proceedings 13th International Conference on Data Engineering, 1997, pp. 497–506.
- [37] Instituto Geográfico Nacional (IGN), Centro Nacional de Información Geográfica (CNIG), Información Geográfica de Referencia, https://centrodedescargas.cnig.es/ CentroDescargas/informacion-geografica-referencia, 2025.
- [38] Gobierno de España, Real decreto 223/2008, de 15 de febrero, bOE núm. 68, de 19 de marzo de 2008, https://www.boe.es/eli/es/rd/2008/02/15/223, 2008.
- [39] A. Hatibovic, Derivation of equations for conductor and sag curves of an overhead line based on a given catenary constant, Period. Polytech. Electr. Eng. Comput. Sci. 58 (2014) 23–27, https://doi.org/10.3311/PPee.6993, https://pp.bme.hu/eecs/ article/view/6993.

- [40] CIGRE Working Group B2.12, Sag tension calculation methods for overhead lines, Tech. Rep. Technical Brochure No. 324, CIGRE, available online 2016, https://www.e-cigre.org/publication/324-sag-tension-calculation-methods-for-overhead-lines.
- [41] Technical Committee 11, Overhead transmission lines Design criteria, IEC Standard IEC 60826:2017, International Electrotechnical Commission, Tech. Rep., 2017, https://webstore.iec.ch/en/publication/33148.
- [42] L.W. Beineke, J.S. Bagga, Line Graphs and Line Digraphs, Developments in Mathematics, vol. 68, Springer International Publishing, Cham, 2021, https://link.springer.com/10.1007/978-3-030-81386-4.
- [43] J.M. Forthofer, B.W. Butler, N.S. Wagenbrenner, A comparison of three approaches for simulating fine-scale surface winds in support of wildland fire management. Part I. Model formulation and comparison against measurements, Int. J. Wildland Fire 23 (7) (2014) 969–981, https://doi.org/10.1071/WF12089, publisher: CSIRO PUB-LISHING, https://www.publish.csiro.au/wf/WF12089.
- [44] N.S. Wagenbrenner, J.M. Forthofer, B.K. Lamb, K.S. Shannon, B.W. Butler, Downscaling surface wind predictions from numerical weather prediction models in complex

- terrain with windninja, Atmos. Chem. Phys. 16 (8) (2016) 5229–5241, https://doi.org/10.5194/acp-16-5229-2016, https://acp.copernicus.org/articles/16/5229/2016/.
- [45] V. Morgan, Thermal Behaviour of Electrical Conductors: Steady, Dynamic, and Fault-Current Ratings, Electronic & Electrical Engineering Research Studies: Lines and Cables for Power Transmission Series, Research Studies Press, 1991, https://books.google.es/books?id=ruNSAAAAMAAJ.
- [46] CIGRÉ Working Group B2.42, Guide for thermal rating calculations of overhead lines, Technical Brochure 601, CIGRÉ, available from https://e-cigre.org, 2014.
- [47] IEEE, 738-2023 IEEE Standard for Calculating the Current-Temperature Relationship of Bare Overhead Conductors, Tech. Rep. IEEE Std 738-2023 (Revision of IEEE Std 738-2012), IEEE, 2023, 10.1109/IEEESTD.2023.10382442.
- [48] T.L. Saaty, The Analytic Hierarchy Process: Planning, Priority Setting, Resource Allocation, McGraw-Hill, New York, 1980.